Understanding the Origin and Implication of the Indirect-to-Direct Bandgap Transition in Multilayer InSe

Nicholas A. Pike[1, 2*], Ruth Pachter[1*], Michael A. Altvater[1,2], Chris Stevens[3,4], Matthew Klein[3,4], Joshua R. Hendrickson[4], Huairuo Zhang[5,6], Sergiy Krylyuk[6], Albert V. Davydov[6], and Nicholas R. Glavin[1]

[1]Air Force Research Laboratory, Materials and Manufacturing Directorate, Wright-Patterson Air Force Base, Ohio, 45433 USA
[2]UES, Inc. 4401 Dayton Xenia Rd. Dayton, Ohio 45432 USA
[3]KBR, Inc. Beavercreek, OH 45431
[4]Air Force Research Laboratory, Sensors Directorate, Wright-Patterson Air Force Base, Ohio, 45433 USA
[5]Theiss Research, Inc., La Jolla, CA 92037, USA
[6]Materials Science and Engineering Division, National Institute of Standards and Technology, Gaithersburg, MD 20899, USA

ABSTRACT: Indium selenide (InSe) multilayers have attracted much interest recently due to their electronic and optical properties, partially dependent on the existence of an indirect-to-direct bandgap transition that is correlated to the multilayer thickness. In this work, we investigate stacks of van der Waals-bonded multilayer InSe, ordered similarly to the γ phase of bulk InSe. We analyze the indirect-to-direct bandgap transition using first-principles methods, identifying the structural changes in the multilayer structures that cause the electronic modifications that result in this transition. We highlight differences between InSe and transition metal dichalcogenides. Our calculations confirm the thickness dependence of the cross-over between the indirect and direct bandgaps in multilayer InSe and emphasize changes in the structure and orbital nature of the valence and conduction bands. The optical spectra predictions performed at a high level of theory are compared to our thorough experimental photoluminescence characterization of our high-quality γ phase bulk InSe. These predictions are correlated to electronic transitions and elucidate the relative contributions of in-plane and out-of-plane dipoles. The insights gained from our study could contribute to the design of multicomponent heterostructures with InSe for future electronic and electrooptical devices.

1. Introduction

The discovery of graphene [1] ushered in an era of atomically thin materials discovery. Since then, there has been a surge of interest in utilizing anisotropic crystals with strong in-plane atomic bonds and weak out-of-plane van der Waals (vdW) interactions. Recently, indium selenide (InSe) has garnered significant attention because of its high electron mobility [2], which overcomes limitations in the use of transition metal dichalcogenides (TMDs) for field-effect transistors [3]. Additionally, it exhibits promising optical properties, including nonlinear responses [4-6]. As a bulk material, InSe is known to exist in four distinct polytypes ($\beta,\ \gamma,\ \delta,\ \varepsilon$) composed of Se-In-In-Se quad-layers [2, 7]. The polytypes are related through the stacking of individual quad-layers with in-plane translations and/or 180° rotations [8] (see Figure 1). Experimentally, optical bandgaps of ca. 1.3 eV were measured [4, 9]. Notably, monolayer and few-layer InSe demonstrated a transition from an indirect to a direct bandgap as the thickness of the layered structure increased, both experimentally [10, 11] and theoretically [12]. Mexican-hat-shaped valence bands and van Hove singularities in the density of states were also demonstrated [13]. However, understanding of the mechanism underlying this transition is lacking.

Here, we present a theoretical investigation of the electronic and optical properties of monolayer, multilayer, and bulk InSe systems, with particular emphasis on changes due to an increase in the number of layers (n_l) (i.e., $n_l = 1 \rightarrow \infty$). We employ density functional theory (DFT) and photoluminescence measurements for bulk γ-InSe. We investigate multilayer structures with the stacking sequence of the γ polytype of InSe, which was confirmed in our experimental characterization, and was also demonstrated to be the most stable

* Nicholas.Pike.3.ctr@us.af.mil * Ruth.Pachter.1@us.af.mil

through first-principles calculations [7]. Previous DFT studies have examined twisted InSe bilayers [14, 15] or multilayers stacked in the β polytype [16, 17].

We begin with a description of the computational and experimental methods in Section 2. This is followed by a discussion of the results in Section 3, divided into sub-sections by n_l. We find that the transition from an indirect to a direct bandgap in multilayer InSe is caused by compression of the intralayer spacing, which in turn influences the orbital characteristics of the electronic bands at specific momentum points in the Brillouin zone, thereby affecting the electronic properties. Interestingly, our results indicate a difference between multilayer InSe and TMD structures in the mechanism driving the compression of the intralayer spacing. Our analysis provides insight into the potential engineering of InSe as a component in few-layer heterostructure field-effect transistors [18].

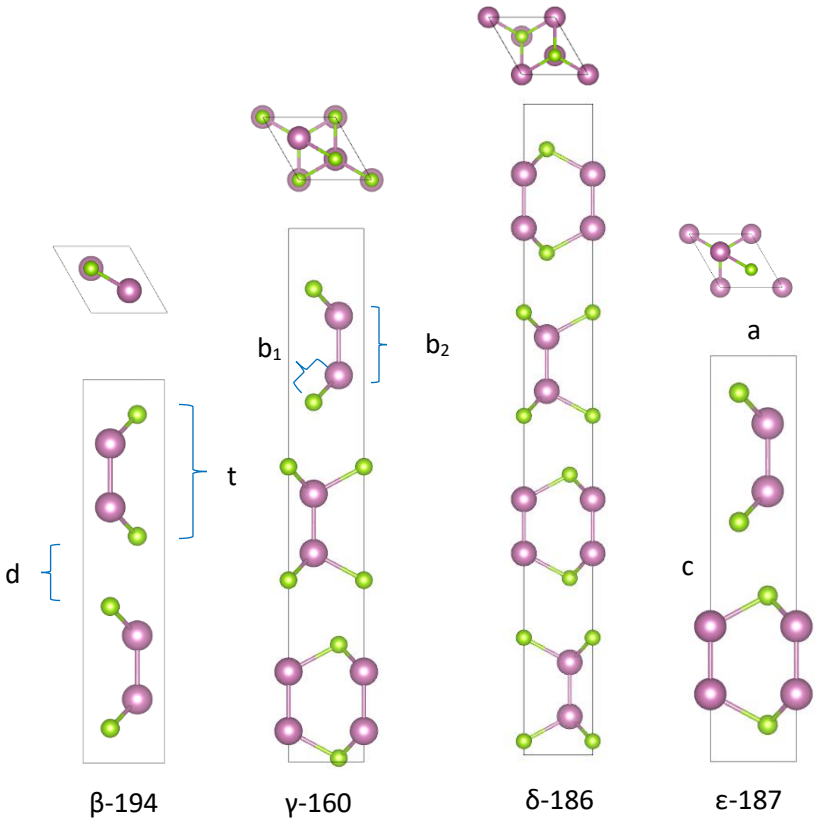

Figure 1: Cartoon images depicting the crystal structures of the four polytypes of InSe, identified by corresponding space group numbers. The boxes represent the unit cell of each polytype, with In and Se denoted by purple and green balls, respectively. The a and c lattice parameters for each polytype are also indicated, as well as the interlayer spacing (d) and intralayer spacing (t).

2. Methods

Computational details. DFT calculations were performed using the Vienna ab initio simulation package [19-21] (VASP). The projector-augmented wave (PAW) method [22] is utilized to model the behavior of the core electrons [23]. The relaxation of each structure involves optimizing the lattice parameters and the internal positions of the atoms using conjugate-gradient algorithms [24]. The Perdew-Burke-Ernzerhof (PBE) exchange-correlation functional within the generalized gradient approximation (GGA) [25] along with a correction for van der Waals (vdW) interactions using the D3 parametrization (vdW-D3) [26] were utilized. The total energy and lattice parameters of the system were determined once the unit cell was fully relaxed. During all self-consistent calculations, total energy convergence was achieved when the difference in the total energy between steps was less than 0.001 meV. To appropriately describe the electronic

interactions and determine the energy cutoff and Monkhorst-Pack [27] mesh of k-points, we conducted convergence calculations for each case, utilizing the maximum value of energy cutoff (ecut) of 450 eV and the highest k-point density (12 points per Å). Spin-orbit coupling (SOC) was used as indicated.

G_0W_0 [28, 29] calculations were performed to model the fundamental bandgap, utilizing the ground-state PBE+vdW-D3 optimized structure as the basis for our single-shot GW calculations. We tested the results for bulk and monolayer InSe and found it necessary to use at least twice as many conduction bands as valence bands, set a response function cut-off energy of $2/3$ ecut, and ensure that no additional iterations of G or W were required to converge the bandgap value. Memory and time constraints limited the number of momentum points considered during the GW calculation. The number of momentum points was equal to $2/3$ of the previously given k-point mesh when SOC was excluded, and to $1/2$ the previously used k-point mesh when SOC was included. We studied the complex frequency-dependent dielectric function using G_0W_0-Bethe-Salpeter (G_0W_0-BSE) calculations [30, 31], utilizing single-shot GW wavefunctions and their derivatives, along with the diagonal elements of the W matrix. The methods described in reference [32] were used to calculate the total linear optical absorption. We tested the convergence of the G_0W_0-BSE calculations by iteratively increasing the number of valence bands (n_v) and conduction (n_c) bands included in BSE summations without SOC, while limiting the included excitations to less than 8 eV. We found that with $n_c, n_v = 12, 16$ and limiting the energy to 8 eV results in a well-converged absorption spectrum below 5 eV for all n_l. When using SOC, we doubled n_v and n_c. The Heyd-Scuseria-Ernzerhof (HSE) [33, 34] functional was also used, as indicated, to compare to our single-shot GW calculations. In all cases, our HSE calculations utilized the relaxed geometry from a PBE+vdW-D3 calculation as a starting point.

Crystal growth. Nominally undoped InSe single crystals were grown by the vertical Bridgman method using a non-stoichiometric polycrystalline $In_{1.04}Se_{0.96}$ charge. The InSe charge was vacuum-sealed in a graphitized quartz ampoule. The melt was equilibrated at 720 °C for several hours, and then the ampoule was translated across a temperature gradient at a rate of 0.5 mm/h.

Powder X-Ray Diffraction. PXRD measurements were collected at room temperature using a Bruker D8 Advance diffractometer (Bruker AXS, Inc., Billerica, MA) equipped with an EIGER2 R 500 K (Dectris, Inc., Philadelphia, PA) single-photon-counting detector. PXRD data were acquired on finely ground InSe powder using Cu Kα (λ= 0.15418 nm) radiation in the 2θ-angle range of 15° to 100°. The patterns were analyzed using commercial MDI Jade version 6.5 software to refine the unit cell parameters (see Figure S1 in Supporting Information).

Scanning transmission electron microscopy (STEM). Samples for plain-view STEM were exfoliated from the InSe flake to take the [001] zone-axis data. Cross-sectional STEM samples were prepared with an FEI Helios NanoLab 660 DualBeam (SEM/FIB) to take the [100] and [1-10] zone-axes data. An FEI Titan 80-300 probe-corrected STEM/TEM microscope operating at 300 keV was employed to conduct atomic resolution annular dark-field scanning transmission electron microscopy (ADF-STEM) imaging analysis, with a probe convergence semi-angle of 14 mrad and a collection angle of 34 mrad to 195 mrad.

Optical measurements. The low temperature photoluminescence (PL) measurements were performed using a PicoQaunt 470nm diode laser operating in CW mode with an average power of 15 μW. The exfoliated ≈100 μm thick single-crystalline flake was mounted in a Montana Instruments S200 cryostation and held at 4 K. The laser was focused onto the sample with a 0.75 NA *in-situ* microscope objective to a spot size of ≈1 μm. The resulting PL was collected through the same objective and guided towards a Princeton Instruments Acton 2750 grating spectrometer with a 300 grooves/mm grating. The collection time used was 1 s for the 850 nm to 1000 nm spectral range and 30 s for the 450 nm to 850 nm range. The dispersed photoluminescence was then measured with a Princeton Instruments PyLoN BR eXcelon CCD.

Refractive index and absorptive properties were obtained by using a variable angle spectroscopic ellipsometer (J. A. Woolam RC2) at room temperature under ambient conditions. The spectral range covered by the instrument was 1 eV to 6 eV with an acquisition time of 10 s. This provides large range of dielectric properties from the UV spectrum to the near-IR. Obtained data was modeled treating the bulk crystal as a substrate and using the general oscillator model with an additional Gaussian, Tauc-Lorentz, and Psemi-M0 term. Surface roughness and index non-uniformity were allowed to be fit; however, their inclusion did not contribute significantly to the fit and the corresponding optical properties. The ellipsometry data is summarized in Figure S2.

3. Results and Discussion

3.1 $n_l = \infty$: Bulk InSe

First, we review the structural and electronic properties of bulk InSe in Table 1. The $\beta, \varepsilon,$ and γ polytypes are known experimentally, and their lattice parameters have been measured by electron diffraction [35]. Lattice parameters and the electronic bandgap for the δ polytype were determined through first-principles calculations [36]. Optical bandgaps between 1.2 eV and 1.4 eV were measured for the $\beta, \varepsilon,$ and γ polytypes utilizing linear absorbance [9, 37, 38]. Our PBE+vdW-D3 calculations of the structural and electronic properties demonstrate underestimation of the bandgap, as expected, but these results can be used to qualitatively understand the electronic spectra and determine the orbital nature of the electronic bands near the Fermi energy. We show the electronic band structures for the four polytypes along their high-symmetry paths in momentum space in Figure S3. Similar bandgap magnitudes, located at either the **Γ** or ***B*** momenta points (B=(0 0 ½)), are indicated. In investigating the orbital nature of each band, we find that the conduction and valence bands near the Fermi energy exhibit the same atomic and orbital characteristics. For example, the first conduction band is a combination of In s orbitals and Se p_z orbitals, while the first valence band is a combination of p_z orbitals from both In and Se. Significant p_x and p_y contributions originate from lower valence bands and higher conduction bands. The inclusion of SOC will affect the lower valence bands and higher conduction bands, thereby influencing the position and intensity of peaks in the optical spectra.

Table 1: Material properties of the polytypes of bulk InSe. "D" corresponds to materials with a direct bandgap energy, while "I" indicates an indirect bandgap energy. Our calculated results are displayed on the second row for each polytype. ** corresponds to our experimental work.

	Symmetry	**a (Å)**	**c (Å)**	**E_g (eV)**				
				PBE+vdw	**HSE**	**G_0W_0**	**G_0W_0 + SOC**	**Exp.**
β	D_{6h}^4, 194, $P6_3/mmc$ [36]	4.05 [35]; 4.0055 [36]; 3.98 [16]; 4.002 [9]	16.93 [35]; 16.9944 [36]; 16.98 [16]; 17.160 [9]	1.348 [9]; 0.53 [16]	1.172 D [36]; 1.84 [16]; 1.39 [17]	1.348 [9]	1.1 [39]	1.2 [39]
		4.08	16.82	0.231		1.33	1.11	
ε	D_{3h}^1, 187, $P\bar{6}m2$ [36]	4.05 [35]; 4.0100 [36]	16.93 [35]; 16.8402 [36]		1.198 I [36]			1.4 I [37]
		4.08	16.717	0.180		1.24	1.01	
γ	C_{3v}^5, 160, R3m [36]	4.00 [35]; 4.0102 [36]; 4.002 [40]	25.32 [35]; 25.1718 [36]; 24.961 [40]		1.132 D [36]	1.00 [41]	1.3 [39]; 1.24 [42]	1.25 [43]; 1.29 D [38]; 1.35 [44]; 1.236 [45]; 1.349 [46]

		4.08; 4.010**	25.076; 24.976**	0.190		1.03	0.95	1.355**
δ	C_{6v}^4, 186, $P6_3mc$ [36]	4.0080 [36]; 4.0100 [36]	33.820 [36]; 33.8200 [36]		1.151 D [36]	1.151 [36]		
		4.08	33.538	0.208		1.10	1.01	

To predict the frequency-dependent dielectric function in comparison to our experimental PL measurement, we employ single-shot GW calculations, initiated from the PBE+vdW-D3 ground state, with and without SOC, as shown in Figure 2 for each of the bulk phases. The energies for the first three exciton peaks, identified based on the first three local maxima of the calculated imaginary part of the dielectric function, are summarized in Table 2, and are correlated to electronic transitions observed in the electronic spectra at Γ (for the $\beta, \varepsilon,$ and δ phases) or at B (for the γ phase). We analyzed the contribution of in-plane or out-of-plane dipole matrix elements, as evaluated from the calculated complex dielectric tensor, demonstrating that the A peak for all bulk phases arises primarily from out-of-plane dipole matrix elements, with minimal contribution from in-plane dipole matrix elements. The B and C peaks for all bulk phases have contributions from both in-plane and out-of-plane dipole matrix elements, with the out-of-plane contribution being several times larger than the in-plane contribution.

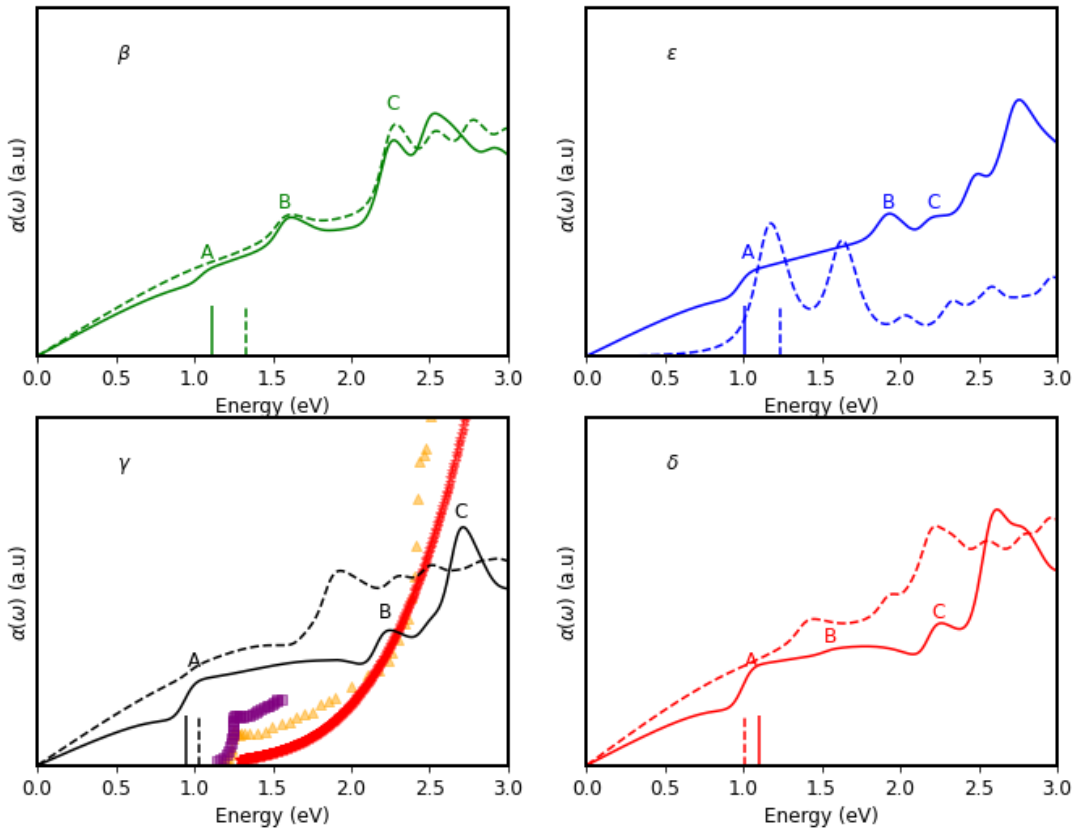

Figure 2: Calculated linear optical absorption spectra using the frequency-dependent GW-BSE dielectric function for four bulk phases of InSe, identifying the A, B, and C peaks. Each linear absorption plot displays the first three peaks with SOC (solid lines), and results without SOC are denoted by dashed lines. Experimental absorption measurements for γ InSe are from reference [48] (orange triangles), reference [35] (purple squares), and our measurements are indicated by red stars. The short vertical solid lines indicate the calculated value of the quasiparticle bandgaps.

Table 2: Energies of exciton peaks in the absorption spectra. The values in parentheses indicate the corresponding results when excluding SOC. *Phase unknown experimentally. **Our experimental measurement.

	Identifier	Energy (eV)	E_{exp} (eV)	E_{lit} (eV)
$\boldsymbol{\beta}$	A	1.04 (1.54)		1.328 [9]
	B	1.54 (2.23)		
	C	2.22 (2.46)		
$\boldsymbol{\varepsilon}$	A	0.98 (1.14)		1.20* [35]
	B	1.89 (1.60)		
	C	2.17 (2.03)		
$\boldsymbol{\gamma}$	A	0.95 (0.97)	1.345**	1.338 [49]; 1.320 [48]; 1.335[47]; 1.20* [35]; 1.338 [45]
	B	2.18 (1.85)	2.078**	2.45 [50]; 2.5 [8]
	C	2.66 (2.25)		
$\boldsymbol{\delta}$	A	1.01 (1.37)		
	B	1.51 (1.91)		
	C	2.20 (2.16)		

Upon inclusion of SOC, our results still underestimate the A peak of the γ phase, while overestimating it for the β phase. We note that the measured B peak energy for the γ phase is in slightly better agreement with our calculated result when excluding SOC. The vertical solid or dashed lines correspond to the calculated G_0W_0 fundamental gap with or without SOC, respectively. Using the position of the A exciton peak and the calculated fundamental gap, we find that with SOC, the calculated exciton binding energies are 64 meV for the β phase, 28 meV for the ε phase, 5 meV for the γ phase, and 2 meV for the δ phase.

Experimentally, we analyzed the temperature-dependent PL spectroscopy of bulk γ phase InSe from 4 K to 300 K for comparison to calculated results regarding the absorption spectrum and the exciton binding energy. First, we note that powder X-ray diffraction (PXRD) (given in Figure S1) and atomically resolved scanning transmission electron microscopy (STEM) along the [001], [100], and [1-10] zone axes (Figure 3a, b, and c, respectively) confirm the γ phase. At 4 K, the PL spectrum (Figure 3d) shows a significant response ranging from 1.30 eV to 1.35 eV, with clear peaks corresponding to the A exciton peak at around 1.345 eV, a P-band peak at 1.334 eV, and shallow defect-related peaks between 1.31 eV and 1.33eV, consistent with earlier reports [45, 47-49]. A weaker peak is observed around 2.078 eV, which is attributed to the B exciton in InSe (Figure 3e). The temperature dependence of the A exciton, B exciton, and P-band peak energies is fitted using an empirical Varshni equation:

$$E_i(T) = E_i(0) - \frac{\alpha T^2}{T+\beta}, \quad (1)$$

where $i = A, B, P$ indexes either the A exciton, B exciton, or P-band energy peak, T is temperature (in K), and α, β are fitting parameters. From the fits using Equation (1) (red lines in Figure 3(f)), we estimate the zero-temperature energies to be $E_A(0) = 1.345$ eV, $E_B(0) = 2.078$ eV, and $E_P(0) = 1.335$ eV for the A exciton, B exciton, and P-band peaks, respectively.

The P-band emission from InSe is a result of an exciton-exciton scattering process, in which one exciton is scattered to higher energy states (near the conduction band edge), while the other is scattered to lower energy, where it recombines to produce light. The P-band emission energy is related to the spacing between Rydberg-like exciton energy levels, and it can be used to measure the exciton binding energy, denoted as E_b, given by [49, 51, 52]

$$E_P = E_A - E_b(1 - 1/n^2) - 3\delta k_B T_{eff} \quad (2)$$

where $n = 1,2,3 \ldots$ is the quantum number of the scattered exciton energy state, δ is a constant less than 1, k_B is the Boltzmann constant, and T_{eff} is an effective exciton temperature. Noting that the free exciton-exciton scattering only occurs when $n = \infty$ and using fitted values for $T = 0$K, we obtain $E_b \approx E_A(0) -$

$E_P(0) = 10$ meV from Equation (2), which is consistent with the commonly reported value of 15 meV [10, 53]. Recent work demonstrated that the exciton binding energy can reach up to 20 meV [49], indicating a significant variability in the experimental determination of E_b. Notably, as recently pointed out (see ref [54] and references therein), the exciton binding energies of bulk 2H TMDs are larger than those of bulk semiconductors, for example, of about 150 meV in 2H-$MoTe_2$ bulk, [55] and therefore may not be fully explained by the material's thickness, as we discuss below. Our calculated exciton binding energy for the bulk γ phase of InSe is smaller yet comparable to the experimentally obtained exciton binding energy of ≈10 meV. The prediction could improve by employing fully consistent GW-BSE calculations, but this is beyond the scope of this study. Moreover, we note that the computations are performed on idealized model systems and do not account fully for the experimental conditions.

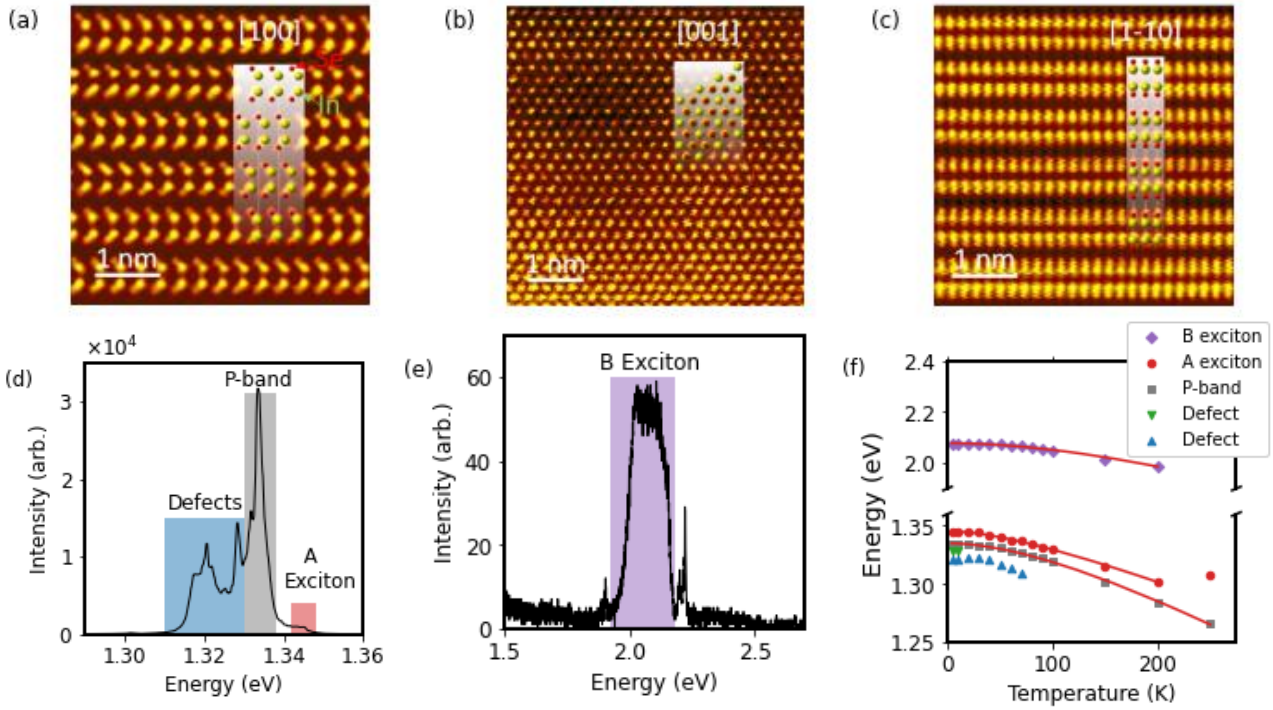

Figure 3: Atomic resolution ADF-STEM characterization of γ-InSe. Atomic images taken along (a) [100], (b) [001], and (c) [1$\bar{1}$0] zone-axis, respectively, match well with the overlapped atomic models of γ -InSe. (d) PL spectrum of the bulk γ phase InSe taken at 4 K in the energy range of 1.29 eV to 1.36 eV with a 1s acquisition time. (e) PL spectrum of bulk γ phase InSe taken at 4K in the energy range of 1.7 eV to 2.7 eV with 30 s acquisition time. (f) Temperature dependence of the PL peaks from InSe. Varshni fits to the P-band, A exciton, and B exciton peak energies vs temperature are shown as red lines.

3.2 $n_l = 1$, Monolayer InSe

Next, we consider monolayer InSe. The relaxed lattice parameters and electronic band structure of monolayer InSe are determined using the PBE+vdW-D3 functional. The results for the lattice parameters are summarized in Table 3, along with the electronic bandgap, incorporating previously published work (e.g., utilizing PBE+vdW-D2 [56]). Calculations using the HSE06 functional were previously reported [39], but the dispersion correction was not considered [13, 16, 57]. The G_0W_0 calculation for the β phase of InSe [39], and the PBE results of references [56] and [39] are consistent with our results.

Table 3: Material properties of monolayer InSe. The thickness, or intralayer spacing, t, of an individual layer is defined in Figure 1. Our calculated values are presented on the second line. The footnotes include the vdW correction, if applicable, and indicate whether SOC was used.

a (Å)	**t (Å)**	**E_g (eV) (PBE)**	**E_g (eV) G_0W_0**	**E_g (eV) (HSE)**
4.093 [13]; 4.05 [16]; 4.09 **[56]**; 4.09 **[58]**; 4.10 **[59]**	5.386 [13]; 5.39 [16] [58]; 5.18 [56]; 5.40 [59]	1.44[a] [56]; 1.52[d] [57]; 1.40 [d, b] [58, 59]; 1.34[d] [16], 1.58[a] [39]	2.97 [39]	2.24 [57]; 2.147 [13]; 2.84 [16, 17]; 2.95[a] [39]
4.077	5.353	1.43[b]	3.03[b]; 3.22[b,c]	2.21[b]

[a] vdW-D2

[b] vdW-D3

[c] +SOC

[d] no London dispersion correction included in the functional

We present the electronic band structure in Figure 4(a). The momentum points corresponding to the bandgap leading to the bandgap transition occur from a point $\boldsymbol{Q}$ in the valence band to the $\boldsymbol{\Gamma}$ point in the conduction band. For monolayer InSe, this $\boldsymbol{Q} \sim (0.1, 0.1, 0.0)$ point becomes closer to the $\boldsymbol{\Gamma}$ point as the number of layers increases (see discussion below) and always lies on the $\boldsymbol{\Gamma K}$ path. We calculate the orbital and atom-specific projection of the converged PBE+vdW-D3 wave function (ϕ_{nk}) as $|\langle Y_{lm}^{\alpha}|\phi_{nk}\rangle|^2$, where Y_{lm}^{α} is the spherical harmonic centered at atom α and l, m are the angular momentum and magnetic quantum numbers that reference the orbit of interest. We found that the valence band at $\boldsymbol{Q}$ is primarily composed of In and Se p_z orbitals, with projections of 0.198 and 0.346, respectively. The conduction band, on the other hand, is mainly composed of In s orbitals with a projection of 0.268, as well as Se s and p_z orbitals with projections of 0.102 and 0.194, respectively.

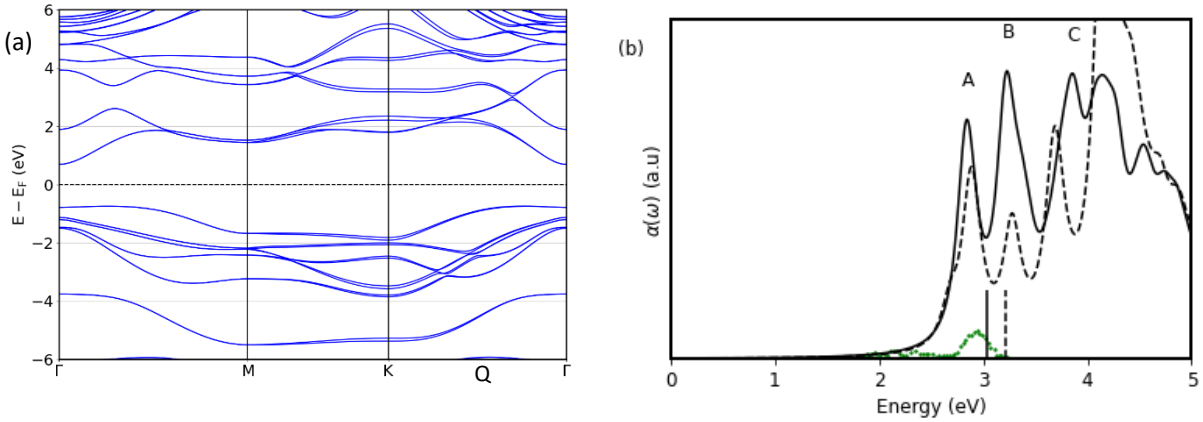

Figure 4: (a) Electronic band structure (PBE+vdw-D3) of monolayer of InSe. The horizontal dashed black line represents the Fermi energy of the system. (b) G_0W_0-BSE absorption spectra with the first three peaks with SOC (dashed line) and without SOC (solid line). The vertical dashed lines in (b) correspond to the calculated indirect G_0W_0 bandgap. Experimental measurements for the B exciton in monolayer InSe from reference [4] are shown in green.

In Figure 4(b), we present the calculated G_0W_0-BSE absorption spectrum of monolayer InSe, computed as the norm of the absorption matrix. The first three peaks without SOC are indicated as A, B, and C, and their peak energies are listed in Table 4. We note that the excitonic behavior at ca. 3.0, blueshifted due to quantum confinement, [10] as measured for the large area monolayer InSe films grown by metal-organic chemical deposition (MoCVD) with low defect density, [41] is consistent with the measurements of mechanically exfoliated InSe that was encapsulated in hexagonal boron nitride. [4] Comparison to literature results on

the imaginary dielectric tensor using the independent particle approximation (IPA) [43] or experimental measurements [4,41] demonstrates that the peak positions calculated with the IPA are red-shifted compared to the experimental data and our GW-BSE calculated results. Our analysis of the absorption matrix components indicates that the A, B, and C peaks (Figure 4b) correspond primarily to in-plane dipole matrix elements, with a minor contribution from the out-of-plane dipole matrix elements.

Table 4: Exciton peaks identified in the frequency-dependent G_0W_0-BSE absorption spectrum in Figure 4(b).

Identifier	**Energy (eV)**	**Energy (eV) w/SOC**	**$E_{lit,\ exp}$ (eV)**	**$E_{lit,DFT}$ (eV)**
A	2.85	2.89	2.25 [60]	2.49 (IPA) [43]
B	3.23	3.275	2.90 [4]; 2.8 [50]	2.73 (IPA) [43]
C	3.86	3.69		2.75 (IPA) [43]

The exciton binding energy E_b is determined by the difference between the direct optical bandgap obtained from our single-shot GW calculation and the energy of the first peak in the GW-BSE absorption spectrum. For monolayer InSe, the direct G_0W_0 bandgap energy without SOC is 3.12 eV, which results in E_b = 0.275 eV. The increase in the exciton binding energy of the monolayer is attributed to quantum confinement and reduced dielectric screening and is comparable in order of magnitude to that of monolayer TMDs, such as monolayer MoS_2 (0.44 ± 0.08 eV) [61] and monolayer $MoTe_2$ (0.58 ± 0.08 eV). [62] Interestingly, in the case of $MoTe_2$, a large exciton binding energy of approximately 300 meV was recently measured also for the multilayer structures, which was rationalized using a Wannier-Mott exciton model. [54] The relationship between the exciton binding energy and the number of layers was given in terms of the exciton radius and the static relative dielectric constant (see ref [54] for details). However, measurements of the exciton binding energy for multilayer InSe are beyond the scope of this study.

3.3 $n_l = 2 - 10$, Multilayer InSe

3.3.1 Structural properties

The structural parameters of the multilayer InSe systems considered here, including the in-plane lattice spacing (a), interlayer spacing (d), intralayer spacing (t), and the bond lengths for In-In and In-Se bonds, are summarized in Figure 5. In multilayer structures, the values of a, d, and t may vary for each layer of the multilayer, resulting in multiple points in the plots in Figure 5. Note that the Se-Se bond lengths are identical to the value of t. We define the thickness of the multilayer systems as the vertical distance between the outermost atoms plus the average interlayer spacing. This definition is consistent with the value obtained in experimental atomic force microscopy (AFM) measurements on 2D materials, where the deflection of the AFM occurs due to forces between the sample and the tip [4, 63]. For example, the reported thickness of the InSe monolayer is ≈0.8 nm [4], 0.832 nm [10], and 0.87 nm [4] while our calculated thickness using this method is 0.84 nm. We illustrate the importance of vdW interactions by comparing our calculated data with and without the vdW-D3 correction to the PBE functional. As the number of layers increases, we observe a divergence in the calculated in-plane lattice parameters (Figure 5(a)) when vdW interactions are excluded (red data points), but convergence when vdW interactions are included. This is also evident in the interlayer spacing (Figure 5(b)), although to a lesser extent. Our findings suggest that it is necessary to include London dispersion in calculations for InSe multilayer systems, similar to bulk InSe [36].

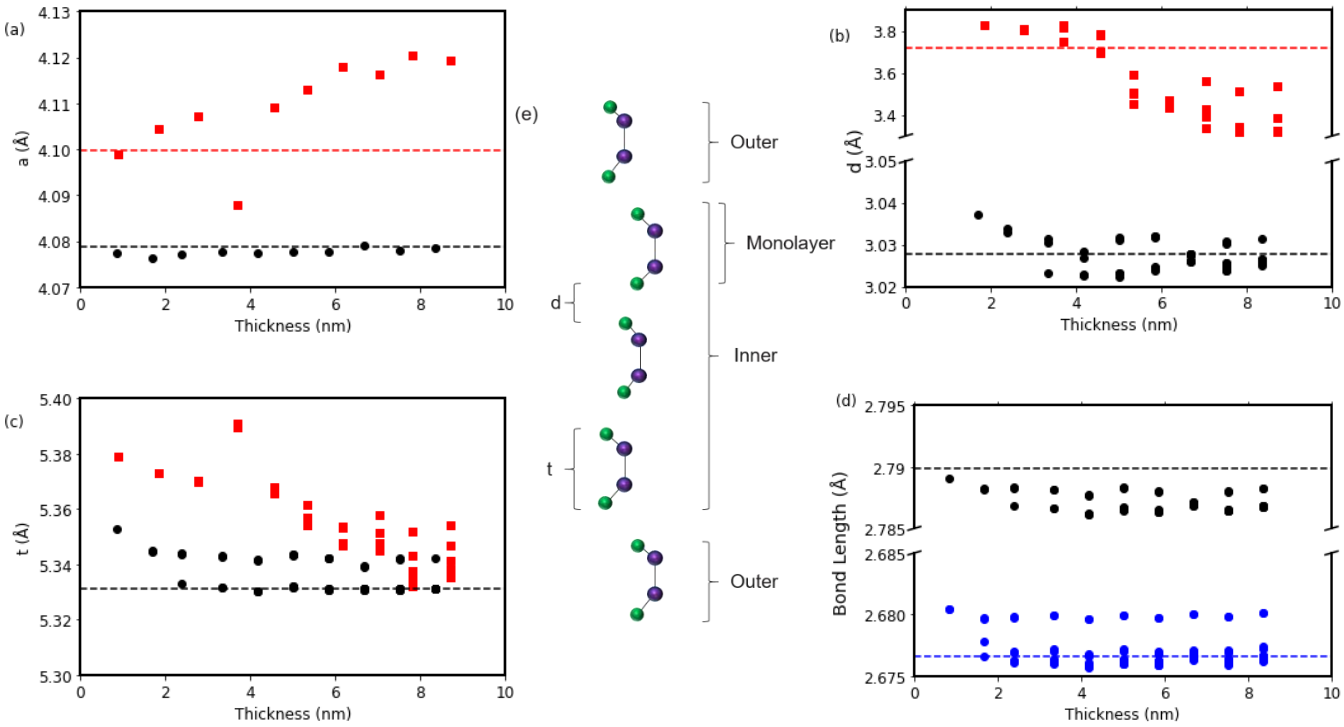

Figure 5: Calculated in-plane lattice spacing *a* (a), interlayer spacing *d* (b), intralayer spacing *t* (c), In-In and In-Se bond lengths (d), and definition of the geometrical parameters (e). Dashed lines correspond to the bulk value using the same approximation. In (a), (b), and (c), black circles represent PBE+vdW-D3 results, while red squares represent calculations without the vdW-D3 correction. In (c), the intralayer spacing *t* is beyond the scale of the Figure when vdW-D3 is excluded. In (d), black circles represent the In-In bond length (b_1) and blue circles the In-Se bond length (b_2), as indicated in Figure 1.

A detailed analysis of the intralayer spacing t, considering the inclusion of vdW interactions in multilayer InSe (Figure 5(c), in black), demonstrates that the interior layers of the structure compress towards the bulk value, while the outer layers of the multilayer stack maintain a "monolayer-like" structure in their thickness (see Figure 5(e) for layer definitions). Similar behavior is observed for the In-Se bond lengths (Figure 5(d), shown in blue), where multiple bond lengths are found for each multilayer. The compression of the interior layers is indicated by a decrease in the In-Se bond length, while the bond length of In-In appears to remain relatively constant as a function of thickness. This compressive behavior indicates that the intralayer interactions become stronger as the number of layers increases, due to increasing In-Se interactions. Such compression of the intralayer spacing does not seem to occur in layered TMDs (denoted MX_2; where M = metal and X = chalcogenide). Previous theoretical studies have shown that the interlayer spacing is compressed through the vdW interaction gap [64]. In layered TMDs, the compression of the structure is driven by X-X interactions, while in InSe, the compression is driven by the M-X interaction. The difference in compression mechanisms can be attributed to the interplay of different layered structures, such as X-M-X in TMDs and X-M-M-X in InSe, as well as differences in the relative strengths of M-M, M-X, and X-X bonds, which stem from the different compositions.

The structural changes calculated upon incorporating vdW interactions in multilayer InSe can explain changes in the band structures, specifically the transition from indirect to direct bandgaps as the material's thickness increases. We find that the first indirect-to-direct bandgap transition occurs when the uppermost valence band, primarily composed of p_z orbitals from Se, decreases in energy until it is below the valence bands composed of p_x and p_y orbitals from Se. Theoretical pressure-dependent investigations of the monolayer of InSe indicate a pressure-induced electronic transition from an indirect to direct bandgap semiconductor at pressures of approximately 8 GPa [59]. We conclude that an increase in pressure leads to

a decrease in the In-In distance, with no significant change in the Se-Se intralayer distance, resulting in the transition from an indirect to direct bandgap. A similar conclusion was reached for bulk γ InSe [65]. As mentioned previously, we have observed a reduction in the intralayer distance due to a decrease in the In-Se bond length in the inner layers of our multilayer structure. This provides additional support for our hypothesis that this change drives the electronic transition.

3.3.2 Electronic properties

Electronic bandgap. Figure 6(a) displays the electronic bandgap results obtained using various approximations, including the PBE functional with and without vdW interactions, and G_0W_0 and HSE calculations with vdW interactions. Here, we demonstrate the decrease in the calculated bandgap as the thickness of the multilayer increases. For both Figures 6(a) and 6(b), we fitted the theoretical and experimental data to the following exponential form:

$$f(l) = \ E_0 - E_1 e^{\left(\frac{-l_0}{l}\right)} \quad (3)$$

where l is the thickness of the multilayer and the coefficients E_0, E_1, and L_0 are reported in Table S1 of the Supporting Information. Note that the calculated bandgap values are adjusted to achieve a bulk bandgap value of 1.25 eV in Figure 6(b) as $l \rightarrow \ \infty$.

Using Equation (3), we determine the intersection points of the direct and indirect bandgap curves by separate fitting. The intersection points indicate that the indirect-to-direct bandgap transition is expected to occur at a thickness greater than 80 nm when employing PBE+vdW-D3, at 6.7 nm for our G_0W_0 calculations, and at 4.3 nm using HSE. When comparing the results to the experimentally determined value of 5 nm [10], we emphasize the importance of accounting for electronic correlation and benchmarking the level of theory in comparison to experimental data.

A fit to the known experimental data for multilayer systems using Equation (3) is shown in Figure 6(b) (solid black line, $r^2 = 0.94$), demonstrating agreement across the range of multilayer materials. The differences can be attributed, in part, to measurements taken on thicker InSe flakes. Note that a scissor correction of approximately 0.9 eV was applied to shift the calculated electronic bandgap data, ensuring that the extrapolated curves reflect the correct bulk bandgap. For our data (grey triangles in Figure 6(b)), we applied a scissor correction of 0.937 eV. The red solid line in Figure 6(b) represents a fit using a quantum well model with a constant energy offset, as proposed in reference [66] (i.e. $E_g = \frac{a}{l^2} + b$). This model, when compared to the data of reference [61], results in $r^2 = 0.29$. Thus, at thicknesses larger than ≈ 5 nm, the quantum well model fits well, but at distances less than 5 nm, the inverse square law for the energy dependence is not applicable due to quantum confinement.

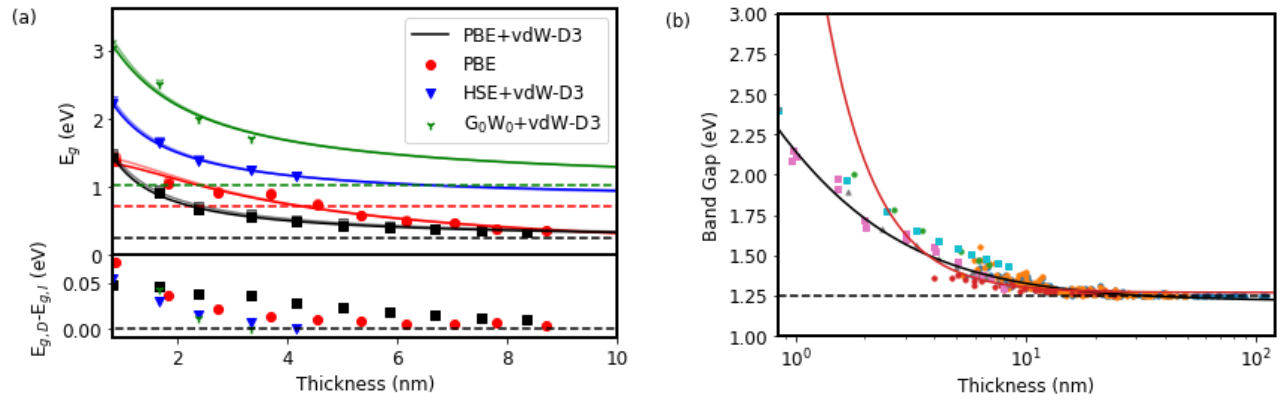

Figure 6: (a) (Upper plot) Calculated direct and indirect electronic bandgap energies at different levels of theory as a function of the multilayer thickness. The horizontal dashed lines correspond to the bulk values obtained using the methods indicated in the figures. (Lower plot) The difference between the value of the direct and indirect bandgap for the indicated method. The black dashed line represents zero difference. (b) Theoretical and experimental values of the bandgap energy as a function of multilayer thickness. The solid black curve represents a fit to experimental values indicated by colored circles (green [4], blue [10], orange [39], and red [61]). Calculated data is shown with colored squares (pink [11], cyan [12], and our calculations in grey without SOC). The red solid line indicates the proposed fit in reference [61], and the black squares in (a) are shifted as described in the text. The black dashed line in (b) represents the unshifted calculated bandgap of bulk γ InSe.

Electron orbital analysis. The electronic band structure of multilayer InSe exhibits a "Mexican-hat"-shaped [12] valence band around **Γ**, with an asymmetry in the valence band profile along the $\boldsymbol{\Gamma - M}$ and $\boldsymbol{\Gamma - K}$ momentum paths, as depicted in Figure 4(a). The maximum of the uppermost valence band has a momentum position at **Q**, which changes as a function of the number of layers, moving towards **Γ** as the number of layers increases (see Figure S4, where the arrow indicates the direction of the movement for all calculation types). Our calculations using PBE+vDW-D3 (in blue), HSE (in red), and G0W0 (in green) all show the movement of the valence band maximum towards **Γ** as the number of layers increases. Given the resolution of our k-point sampling (which is dependent on the calculation) along the path **Γ*K***, we note that some of the multilayers have the same momentum points. All our G_0W_0 momentum points lie along the x-axis because of the density of k-points used in the calculation.

In Figure 7, we plot the total orbital projection of the indicated orbitals for the valence band at **Q** (left panel of Figure 7) and of the conduction band at **Γ** (right panel of Figure 7). In γ InSe, the electronic bandgap energy occurs at the B momentum point, which in the two-dimensional limit, becomes **Γ**. Other orbits with orbital projections of less than 0.05 are not shown in Figure 7. The dominant orbital projections for monolayer of InSe, at a specific thickness of ~0.8 nm, show good agreement with the calculated orbital projections using HSE [53]. As the number of layers increases, we observe that the orbital projections approach their respective bulk limit, as indicated by the dashed lines in Figure 7.

We find that the average In-In, In-Se, and Se-Se bond lengths at every thickness and the orbital projections (Figure 7) are correlated. In particular, we observe a Pearson correlation of 0.78 between the In-In average bond length and the valence band indium p_z orbital projection, a Pearson correlation of 0.83 between the In-Se average bond length and the valence band selenium p_z orbital projection, and a Pearson correlation of 0.54 for the Se-Se average bond length and the conduction band selenium p_z orbital. The Pearson correlations show a negative association between the average Se-Se bond length and three orbital projections: the valence band selenium p_z, and the conduction band indium and selenium s orbital projections (-0.66, -0.51, and -0.52, respectively). The remaining correlation pairs have Pearson correlation values that are insignificant.

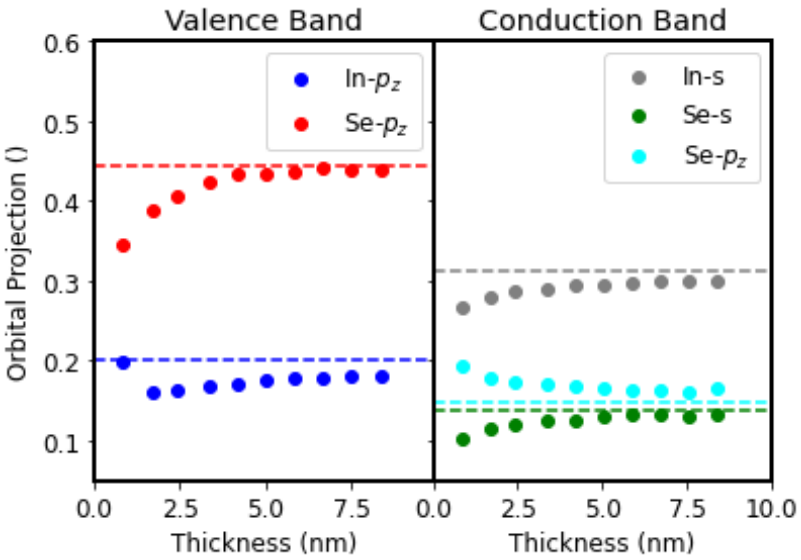

Figure 7: Calculated total orbital projections of the wave function using PBE+ vdW-D3, for the appropriate spherical harmonic for each atom and the identified orbitals. Orbital projections less than 0.05 are not shown for clarity and the orbital projection of bulk γ InSe are indicated as dashed lines for the specified orbitals.

4. Conclusions

In this investigation, we analyzed the γ phase of bulk InSe theoretically and experimentally, demonstrating consistency in the optical properties, and in addition, the monolayer and multilayer structures, with special emphasis on understanding the origin of the indirect-to-direct bandgap transition in multilayer InSe. Using first-principles methods we investigated stacks of van der Waals-bonded multilayer InSe, ordered similarly to the γ phase of bulk InSe. We identified the relevant structural modifications in the multilayers that cause the indirect-to-direct bandgap transition, also in comparison to 2D TMDs. Specifically, we found that as the thickness approaches the bulk limit, the intralayer spacing shortens, approaching the bulk material. As a result of this structural change, the momentum point **Q** shifts towards Γ with an increasing contribution of In and Se p_z orbitals, leading to a transition to a direct bandgap. Employing GW-BSE calculations, we determined the relative contribution of in-plane and out-of-plane dipoles, correlating with the electronic transitions. The study confirms that the indirect-to-direct bandgap transition in multilayer InSe depends on the thickness. Furthermore, we demonstrate by GW and HSE calculated results that this crossover occurs at ca. 5 nm and 4 nm thickness, respectively. This result is in good agreement with experimental findings. Our calculations provide the theoretical basis for future investigation of few-layer InSe heterostructures in field-effect transistors.

DATA AVAILABILITY STATEMENT

The data used is available upon request from the corresponding author.

SUPPORTING INFORMATION

The Supporting Information is available free of charge at https://pubs.acs.org/doi/10.1021/acs.jpcc.4c01104. Fit of the bandgap of multilayer InSe to the thickness; powder XRD scan for bulk γ InSe; refractive index of bulk γ InSe from room temperature variable angle spectroscopic ellipsometry; electronic band structures of bulk phases of InSe; and momentum components of the layer-dependent maximum of the valence band at Q

■ AUTHOR INFORMATION

Corresponding Authors

Nicholas A. Pike − Air Force Research Laboratory, Materials and Manufacturing Directorate, Wright-Patterson Air Force Base, Ohio 45433, United States; UES, Inc., Dayton, Ohio 45432, United States; orcid.org/0000-0002-4221-4037;

Email: Nicholas.pike.3.ctr@us.af.mil

Ruth Pachter − Air Force Research Laboratory, Materials and Manufacturing Directorate, Wright-Patterson Air Force Base, Ohio 45433, United States; Email: Ruth.Pachter.1@us.af.mil

Authors

Michael A. Altvater − Air Force Research Laboratory, Materials and Manufacturing Directorate, Wright-Patterson Air Force Base, Ohio 45433, United States; UES, Inc., Dayton, Ohio 45432, United States

Christopher E. Stevens − KBR, Inc., Beavercreek, Ohio 45431, United States; Air Force Research Laboratory, Sensors Directorate, Wright-Patterson Air Force Base, Ohio 45433, United States; orcid.org/0000-0002-5509-8610

Matthew Klein − KBR, Inc., Beavercreek, Ohio 45431, United States; Air Force Research Laboratory, Sensors Directorate, Wright-Patterson Air Force Base, Ohio 45433, United States

Joshua R. Hendrickson − Air Force Research Laboratory, Sensors Directorate, Wright-Patterson Air Force Base, Ohio 45433, United States; orcid.org/0000-0002-5342-0346

Huairuo Zhang − Theiss Research, Inc., La Jolla, California 92037, United States; Materials Science and Engineering Division, National Institute of Standards and Technology, Gaithersburg, Maryland 20899, United States; orcid.org/0000-0002-1984-1200

Sergiy Krylyuk − Materials Science and Engineering Division, National Institute of Standards and Technology, Gaithersburg, Maryland 20899, United States; orcid.org/0000-0003-4573-9151

Albert V. Davydov − Materials Science and Engineering Division, National Institute of Standards and Technology, Gaithersburg, Maryland 20899, United States

Nicholas R. Glavin − Air Force Research Laboratory, Materials and Manufacturing Directorate, Wright-Patterson Air Force Base, Ohio 45433, United States

ACKNOWLEDGMENTS

We acknowledge helpful support and resources from the DoD High-Performance Computing Modernization Program. S.K. and A.V.D. acknowledge support from the Material Genome Initiative funding allocated to NIST. H.Z. acknowledges support from NIST Cooperative Agreement #70NANB22H101.

Disclaimer: Certain commercial equipment, instruments, software, or materials are identified in this paper in order to specify the experimental procedure adequately. Such identifications are not intended to imply recommendation or endorsement by NIST, nor it is intended to imply that the materials or equipment identified are necessarily the best available for the purpose.

■ REFERENCES

(1) Novoselov, K. S.; Geim, A. K.; Morozov, S. V.; Jiang, D.; Zhang, Y.; Dubonos, S. V.; Grigorieva, I. V.; Firsov, A. A. Electric field effect in atomically thin carbon films. Science 2004, 306 (5696), 666−669.
(2) Boukhvalov, D. W.; Gürbulak, B.; Duman, S.; Wang, L.; Politano, A.; Caputi, L. S.; Chiarello, G.; Cupolillo, A. The advent of indium selenide: Synthesis, electronic properties, ambient stability and applications. Nanomaterials 2017, 7 (11), 372.
(3) Jiang, J.; Xu, L.; Qiu, C.; Peng, L.-M. Ballistic two-dimensional InSe transistors. Nature 2023, 616 (7957), 470−475.
(4) Bandurin, D. A.; Tyurnina, A. V.; Yu, G. L.; Mishchenko, A.; Zolyomi, V.; Morozov, S. V.; Kumar, R. K.; Gorbachev, R. V.; Kudrynskyi, Z. R.; Pezzini, S.; Kovalyuk, Z. D.; Zeitler, U.; Novoselov, K. S.; Patane, A.; Eaves, L.; Grigorieva, I. V.; Fal'ko, V. I.; Geim, A. K.; Cao, Y. High electron mobility, quantum Hall effect and anomalous optical response in atomically thin InSe. Nat. Nanotechnol 2017, 12 (3), 223−227.
(5) Song, C.; Huang, S.; Wang, C.; Luo, J.; Yan, H. The optical properties of few-layer InSe. J. Appl. Phys. 2020, 128 (6), No. 060901.
(6) Chen, C.; Dong, N.; Huang, J.; Chen, X.; Wang, H.; Wang, Z.; Wang, J. Nonlinear optical properties and ultrafast carrier dynamics of 2D indium selenide nanosheets. Adv. Opt. Mater. 2021, 9 (24), No. 2101432.
(7) Sun, Z.; Zhang, Y.; Qian, J.; Qiao, R.; Li, X.; Wang, Z.; Zheng, C.; Liu, K.; Cao, T.; Liu, W. T. Compelling Evidence for the ε-Phase InSe Crystal by Oblique Incident Second Harmonic Generation. Adv. Opt. Mater. 2022, 10 (19), No. 2201183.
(8) Gomes da Costa, P.; Dandrea, R. G.; Wallis, R. F.; Balkanski, M. First-principles study of the electronic structure of gamma -InSe and beta -InSe. Phys. Rev. B Condens Matter 1993, 48 (19), 14135−14141.
(9) Gürbulak, B.; Şata, M.; Dogan, S.; Duman, S.; Ashkhasi, A.; Keskenler, E. F. Structural characterizations and optical properties of InSe and InSe:Ag semiconductors grown by Bridgman/Stockbarger technique. Physica E: Low-dimensional Systems and Nanostructures 2014, 64, 106−111.
(10) Mudd, G. W.; Svatek, S. A.; Ren, T.; Patane, A.; Makarovsky, O.; Eaves, L.; Beton, P. H.; Kovalyuk, Z. D.; Lashkarev, G. V.; Kudrynskyi, Z. R.; Dmitriev, A. I. Tuning the bandgap of exfoliated InSe nanosheets by quantum confinement. Adv. Mater. 2013, 25 (40), 5714−5718.
(11) Brotons-Gisbert, M.; Andres-Penares, D.; Suh, J.; Hidalgo, F.; Abargues, R.; Rodriguez-Canto, P. J.; Segura, A.; Cros, A.; Tobias, G.; Canadell, E.; Ordejon, P.; Wu, J.; Martinez-Pastor, J. P.; Sanchez-Royo, J. F. Nanotexturing To Enhance Photoluminescent Response of Atomically Thin Indium Selenide with Highly Tunable Band Gap. Nano Lett. 2016, 16 (5), 3221−3229.
(12) Sánchez-Royo, J. F.; Muñoz-Matutano, G.; Brotons-Gisbert, M.; Martínez-Pastor, J. P.; Segura, A.; Cantarero, A.; Mata, R.; Canet-Ferrer, J.; Tobias, G.; Canadell, E.; Marqués-Hueso, J.; Gerardot, B. D. Electronic structure, optical properties, and lattice dynamics in atomically thin indium selenide flakes, Nano Research, 7 (2014) 1556-1568.
(13) Wan, W.; Zhao, S.; Ge, Y.; Liu, Y. Phonon and electron transport in Janus monolayers based on InSe. J. Phys.: Condens. Matter 2019, 31 (43), 435501.
(14) Kang, P. Indirect-to-direct bandgap transition in bilayer InSe: roles of twistronics. 2D Materials 2020, 7 (2), No. 021002.
(15) Yao, X.; Zhang, X. Electronic Structures of Twisted Bilayer InSe/InSe and Heterobilayer Graphene/InSe. ACS Omega 2021, 6 (20), 13426−13432.
(16) Bejani, M.; Pulci, O.; Karimi, N.; Cannuccia, E.; Bechstedt, F. Electronic structure, vibrational properties, and optical spectra of two and three-dimensional hexagonal InSe: Layer-dependent ab initio calculations. Physical Review Materials 2022, 6 (11), No. 115201.
(17) Sang, D. K.; Wang, H.; Qiu, M.; Cao, R.; Guo, Z.; Zhao, J.; Li, Y.; Xiao, Q.; Fan, D.; Zhang, H. Two Dimensional beta-InSe with Layer-Dependent Properties: Band Alignment, Work Function and Optical Properties. Nanomaterials (Basel) 2019, 9 (1), 82.

(18) Miao, J.; Leblanc, C.; Wang, J.; Gu, Y.; Liu, X.; Song, B.; Zhang, H.; Krylyuk, S.; Hu, W.; Davydov, A. V. Heterojunction tunnel triodes based on two-dimensional metal selenide and three-dimensional silicon. Nat. Electron. 2022, 5 (11), 744−751.
(19) Kresse, G.; Hafner, J. Ab initio molecular dynamics for openshell transition metals. Phys. Rev. B Condens Matter 1993, 48 (17), 13115−13118.
(20) Kresse, G.; Furthmüller, J. Efficiency of ab-initio total-energy calculations for metals and semiconductors using a plane-wave basis set. Comput. Mater. Sci. 1996, 6 (1), 15−50.
(21) Kresse, G.; Furthmüller, J. Efficient iterative schemes for ab initio total-energy calculations using a plane-wave basis set. Phys. Rev. B Condens Matter 1996, 54 (16), 11169−11186.
(22) Blochl, P. E. Projector augmented-wave method. Phys. Rev. B Condens Matter 1994, 50 (24), 17953−17979.
(23) Kresse, G.; Joubert, D. From ultrasoft pseudopotentials to the projector augmented-wave method. Phys. Rev. B 1999, 59 (3), 1758−1775.
(24) Freysoldt, C.; Boeck, S.; Neugebauer, J. Direct minimization technique for metals in density functional theory. Phys. Rev. B 2009, 79 (24), No. 241103.
(25) Perdew, J. P.; Burke, K.; Ernzerhof, M. Generalized Gradient Approximation Made Simple. Phys. Rev. Lett. 1996, 77 (18), 3865− 3868.
(26) Grimme, S.; Antony, J.; Ehrlich, S.; Krieg, H. A consistent and accurate ab initio parametrization of density functional dispersion correction (DFT-D) for the 94 elements H-Pu. J. Chem. Phys. 2010, 132 (15), No. 154104.
(27) Monkhorst, H. J.; Pack, J. D. Special points for Brillouin-zone integrations. Phys. Rev. B 1976, 13 (12), 5188−5192.
(28) Luo, W.; Ismail-Beigi, S.; Cohen, M. L.; Louie, S. G. Quasiparticle band structure of ZnS and ZnSe. Phys. Rev. B 2002, 66 (19), No. 195215.
(29) Oshikiri, M.; Aryasetiawan, F. Band gaps and quasiparticle energy calculations on ZnO, ZnS, and ZnSe in the zinc-blende structure by the GW approximation. Phys. Rev. B 1999, 60 (15), 10754−10757.
(30) Albrecht, S.; Reining, L.; Del Sole, R.; Onida, G. Ab Initio Calculation of Excitonic Effects in the Optical Spectra of Semiconductors. Phys. Rev. Lett. 1998, 80 (20), 4510−4513.
(31) Rohlfing, M.; Louie, S. G. Electron-Hole Excitations in Semiconductors and Insulators. Phys. Rev. Lett. 1998, 81 (11), 2312−2315.
(32) Pike, N. A.; Pachter, R.; Martinez, A. D.; Cook, G. Computational Analysis of the Optical Response of ZnSe with dorbital Defects. J. Phys.: Condens. Matter 2022, 34, 205402.
(33) Heyd, J.; Scuseria, G. E.; Ernzerhof, M. Hybrid functionals based on a screened Coulomb potential. J. Chem. Phys. 2003, 118 (18), 8207−8215.
(34) Krukau, A. V.; Vydrov, O. A.; Izmaylov, A. F.; Scuseria, G. E. Influence of the exchange screening parameter on the performance of screened hybrid functionals. J. Chem. Phys. 2006, 125 (22), 224106
(35) Mancini, A. M.; Micocci, G.; Rizzo, A. New materials for optoelectronic devices: Growth and characterization of indium and gallium chalcogenide layer compounds. Mater. Chem. Phys. 1983, 9 (1−3), 29−54.
(36) Srour, J.; Badawi, M.; El Haj Hassan, F.; Postnikov, A. Comparative study of structural and electronic properties of GaSe and InSe polytypes. J. Chem. Phys. 2018, 149 (5), No. 054106.
(37) Lei, S.; Ge, L.; Najmaei, S.; George, A.; Kappera, R.; Lou, J.; Chhowalla, M.; Yamaguchi, H.; Gupta, G.; Vajtai, R.; Mohite, A. D.; Ajayan, P. M. Evolution of the electronic band structure and efficient photo-detection in atomic layers of InSe. ACS Nano 2014, 8 (2), 1263−1272.
(38) Julien, C. M.; Balkanski, M. Lithium reactivity with III−VI layered compounds. Materials Science and Engineering: B 2003, 100 (3), 263−270.
(39) Debbichi, L.; Eriksson, O.; Lebegue, S. Two-Dimensional Indium Selenides Compounds: An Ab Initio Study. J. Phys. Chem. Lett. 2015, 6 (15), 3098−3103.
(40) Mudd, G. W.; Patanè, A.; Kudrynskyi, Z. R.; Fay, M. W.; Makarovsky, O.; Eaves, L.; Kovalyuk, Z. D.; Zólyomi, V.; Falko, V. Quantum confined acceptors and donors in InSe nanosheets. Appl. Phys. Lett. 2014, 105 (22), 221909.

(41) Song, S.; Jeon, S.; Rahaman, M.; Lynch, J.; Rhee, D.; Kumar, P.; Chakravarthi, S.; Kim, G.; Du, X.; Blanton, E. W.; Kisslinger, K.; Snure, M.; Glavin, N. R.; Stach, E. A.; Olsson, R. H.; Jariwala, D. Wafer-scale growth of two-dimensional, phase-pure InSe. Matter 2023, 6 (10), 3483−3498.
(42) Ferlat, G.; Xu, H.; Timoshevskii, V.; Blase, X. Ab initio studies of structural and electronic properties of solid indium selenide under pressure. Phys. Rev. B 2002, 66 (8), No. 085210.
(43) Brotons-Gisbert, M.; Proux, R.; Picard, R.; Andres-Penares, D.; Branny, A.; Molina-Sanchez, A.; Sanchez-Royo, J. F.; Gerardot, B. D. Out-of-plane orientation of luminescent excitons in two-dimensional indium selenide. Nat. Commun. 2019, 10 (1), 3913.
(44) Manjón, F. J.; Errandonea, D.; Segura, A.; Muñoz, V.; Tobías, G.; Ordejón, P.; Canadell, E. Experimental and theoretical study of band structure of InSe and In1−xGaxSe ($x < 0.2$) under high pressure: Direct to indirect crossovers. Phys. Rev. B 2001, 63 (12), No. 125330.
(45) Camassel, J.; Merle, P.; Mathieu, H.; Chevy, A. Excitonic absorption edge of indium selenide. Phys. Rev. B 1978, 17 (12), 4718−4725.
(46) Madelung, O. Semiconductors: data handbook; Springer Science & Business Media, 2004.
(47) Abay, B.; Efeoğlu, H.; Yoğurtçu, Y. K. Low-temperature photoluminescence of n-InSe layer semiconductor crystals. Mater. Res. Bull. 1998, 33 (9), 1401−1410.
(48) Andriyashik, M. V.; Sakhnovskii, M. Y.; Timofeev, V. B.; Yakimova, A. S. Optical Transitions in the Spectra of the Fundamental Absorption and Reflection of InSe Single Crystals. Phys. Status Solidi (b) 1968, 28 (1), 277−285.
(49) Shubina, T. V.; Desrat, W.; Moret, M.; Tiberj, A.; Briot, O.; Davydov, V. Y.; Platonov, A. V.; Semina, M. A.; Gil, B. InSe as a case between 3D and 2D layered crystals for excitons. Nat. Commun. 2019, 10 (1), 3479.
(50) Song, C.; Fan, F.; Xuan, N.; Huang, S.; Wang, C.; Zhang, G.; Wang, F.; Xing, Q.; Lei, Y.; Sun, Z.; Wu, H.; Yan, H. Drastic enhancement of the Raman intensity in few-layer InSe by uniaxial strain. Phys. Rev. B 2019, 99 (19), No. 195414.
(51) Nakayama, M.; Hirao, T.; Hasegawa, T. Photoluminescence properties of exciton−exciton scattering in a GaAs/AlAs multiple quantum well. Physica E: Low-dimensional Systems and Nanostructures 2010, 42 (10), 2644−2647.
(52) Liang, Y.; Zhao, L.; Li, C.; Du, J.; Shang, Q.; Wei, Z.; Zhang, Q. Strong Exciton-Exciton Scattering of Exfoliated van der Waals InSe toward Efficient Continuous-Wave Near-Infrared P-Band Emission. Nano Lett. 2023, 23 (9), 4058−4065.
(53) Zultak, J.; Magorrian, S. J.; Koperski, M.; Garner, A.; Hamer, M. J.; Tovari, E.; Novoselov, K. S.; Zhukov, A. A.; Zou, Y.; Wilson, N. R.; Haigh, S. J.; Kretinin, A. V.; Fal'ko, V. I.; Gorbachev, R. Ultra-thin van der Waals crystals as semiconductor quantum wells. Nat. Commun. 2020, 11 (1), 125.
(54) Jung, E.; Park, J. C.; Seo, Y. S.; Kim, J. H.; Hwang, J.; Lee, Y. H. Unusually large exciton binding energy in multilayered 2H-MoTe(2). Sci. Rep. 2022, 12 (1), 4543.
(55) Arora, A.; Drüppel, M.; Schmidt, R.; Deilmann, T.; Schneider, R.; Molas, M. R.; Marauhn, P.; Michaelis de Vasconcellos, S.; Potemski, M.; Rohlfing, M. Interlayer excitons in a bulk van der Waals semiconductor. Nat. Commun. 2017, 8 (1), 639.
(56) Sun, C.; Xiang, H.; Xu, B.; Xia, Y.; Yin, J.; Liu, Z. Ab initio study of carrier mobility of few-layer InSe. Applied Physics Express 2016, 9 (3), No. 035203.
(57) Zhou, S.; Liu, C.-C.; Zhao, J.; Yao, Y. Monolayer group-III monochalcogenides by oxygen functionalization: a promising class of two-dimensional topological insulators. npj Quant. Mater. 2018, 3 (1), 16.
(58) Li, W.; Li, J. Piezoelectricity in two-dimensional group-III monochalcogenides. Nano Research 2015, 8 (12), 3796−3802.
(59) Xiong, H.; Li, R.; Cheng, Y.; Xing, G.; Huang, W. Bandgap engineering of layered mono-chalcogenides via pressure. J. Appl. Phys. 2021, 129 (15), No. 155703.
(60) Yang, Z.; Jie, W.; Mak, C. H.; Lin, S.; Lin, H.; Yang, X.; Yan, F.; Lau, S. P.; Hao, J. Wafer-Scale Synthesis of High-Quality Semiconducting Two-Dimensional Layered InSe with Broadband Photoresponse. ACS Nano 2017, 11 (4), 4225−4236.

(61) Hill, H. M.; Rigosi, A. F.; Roquelet, C.; Chernikov, A.; Berkelbach, T. C.; Reichman, D. R.; Hybertsen, M. S.; Brus, L. E.; Heinz, T. F. Observation of Excitonic Rydberg States in Monolayer MoS2 and WS2 by Photoluminescence Excitation Spectroscopy. Nano Lett. 2015, 15 (5), 2992−2997.
(62) Yang, J.; Lu, T.; Myint, Y. W.; Pei, J.; Macdonald, D.; Zheng, J. C.; Lu, Y. Robust Excitons and Trions in Monolayer MoTe2. ACS Nano 2015, 9 (6), 6603−6609.
(63) Jalili, N.; Laxminarayana, K. A review of atomic force microscopy imaging systems: application to molecular metrology and biological sciences. Mechatronics 2004, 14 (8), 907−945.
(64) Pike, N. A.; Dewandre, A.; Chaltin, F.; Garcia Gonzalez, L.; Pillitteri, S.; Ratz, T.; Verstraete, M. J. Spontaneous interlayer compression in commensurately stacked van der Waals heterostructures. Phys. Rev. B 2021, 103 (23), No. 235307.
(65) Olguín, D.; Cantarero, A.; Ulrich, C.; Syassen, K. Effect of pressure on structural properties and energy band gaps of γ-InSe. physica status solidi (b) 2003, 235 (2), 456−463.
(66) Zhao, Q.; Puebla, S.; Zhang, W.; Wang, T.; Frisenda, R.; Castellanos-Gomez, A. Thickness Identification of Thin InSe by Optical Microscopy Methods. Adv. Photonics Res. 2020, 1 (2), No. 2000025.